Faraday Discussions

Cite this: *Faraday Discuss.*, 2015, **180**, 331

PAPER

Determination of the local corrosion rate of magnesium alloys using a shear force mounted scanning microcapillary method†

Philippe Dauphin-Ducharme,[a] W. Jeffrey Binns,[b] Michael E. Snowden,[a] David W. Shoesmith[b] and Janine Mauzeroll*[a]

Received 23rd December 2014, Accepted 16th January 2015
DOI: 10.1039/c4fd00276h

The successful development of scanning probe techniques to characterize corrosion *in situ* using multifunctional probes is intrinsically tied to surface topography signal decoupling from the measured electrochemical fluxes. One viable strategy is the shear force controlled scanning microcapillary method. Using this method, pulled quartz micropipettes with an aperture of 500 nm diameter were used to resolve small and large variations in topography in order to quantify the local corrosion rate of microgalvanically and galvanically corroded Mg alloys. To achieve topography monitoring of corroded surfaces, shear force feedback was employed to position the micropipette at a reproducible working height above the substrate. We present proof of concept measurements over a galvanic couple of a magnesium alloy (AE44) and mild steel along with a microgalvanically corroded ZEK100 Mg alloy, which illustrates the ability of shear force to track small (1.4 μm) and large (700 μm) topographic variations from high aspect ratio features. Furthermore, we demonstrate the robustness of the technique by acquiring topographic data for 4 mm along the magnesium–steel galvanic couple sample and a 250 × 30 μm topography map over the ZEK100 Mg alloy. All topography results were benchmarked using standard optical microscopies (profilometry and confocal laser scanning microscopy).

1 Introduction

Scanning probe techniques (SPTs) have found extensive applications in corrosion science as tools for quantitative and qualitative analyses that can tackle key issues including: the identification of the corrosion initiation sites, predicting the propagation of corrosion, the effectiveness of smart inhibition coatings and lifetime predictions.[1]

[a]*Department of Chemistry, McGill University, 801 Sherbrooke St W., Montreal, Quebec, H3A 0B8, Canada. E-mail: janine.mauzeroll@mcgill.ca; Fax: +1 514 398-6999; Tel: +1 514 398-3898*

[b]*Department of Chemistry and Surface Science Western, Western University, London, Ontario, N6A 5B7, Canada*

† Electronic supplementary information (ESI) available. See DOI: 10.1039/c4fd00276h

Specifically, scanning electrochemical microscopy (SECM) is a highly relevant electroanalytical method to quantify local chemical fluxes *in situ* and to map the heterogeneous electrochemical activity of corroding surfaces.[1–3] A normal SECM setup uses a microelectrode (ME) sensor, included in a four electrode configuration controlled by a bipotentiostat, attached to a 3-axis translator positioning system. The four electrodes required are two working electrodes: ME and substrate/sample, a counter electrode: CE, and a reference electrode: REF. In corrosion studies, SECM offers an arsenal of modes for the direct detection of ionic/molecular fluxes produced at the corroding interface,[3] to probe corrosion mechanisms,[4] coatings[5,6] and surface modifications.[7] Recently, the potentiometric,[8,9] feedback,[10,11] and generation–collection modes[10,12–14] of SECM have been applied to study the corrosion of Mg alloys which, given their light-weight properties and low cost, are of interest for automotive applications.[15]

An important challenge when performing such SECM measurements is the ability to decouple and resolve variations in topography in order to quantify local corrosion rates. In comparison to the detection of electrochemical fluxes, topography sensing is less sensitive but can still provide local corrosion rates that must be in agreement with the chemical fluxes measured at the ME. Simultaneous topography tracking therefore offers an internal data validation. Several strategies have been developed to decouple topography from surface reactivity.[16] Lee *et.* al.[17] attached a tuning fork to a gold ring disk ME, and monitored the mechanical oscillations of this assembly with a pulsed laser. Tuning fork control loops have been successfully applied to complex biological samples[18,19] with topographical variations in the order of 15 μm. Combined atomic force microscopy (AFM)-SECM probes have also been fabricated to assess surface topography along with electrochemical reactivity.[20–22] A maximal depth of 2 μm was measured in these studies. Another strategy involves alternating current scanning electrochemical microscopy (AC-SECM) that relies on impedance measurements to monitor the tip-to-substrate separation.[4] Using AC-SECM, hard substrates, such as corroding copper,[23] Al alloys,[24] stainless steel[4] and substrates with easily deformed features, *e.g.* cells,[25] of less than 20 μm have been imaged. Finally, shear force (SF) control loops are also available and were originally implemented as a method to maintain a constant tip-to-substrate separation during a SECM scan[26] using optical detection.[27] Nowadays, two piezoelectric elements are attached to the shaft of a SECM probe.[28,29] An alternating potential is applied to the piezo furthest from the ME tip (stimulation piezo) which induces a mechanical oscillation of the ME. The piezo element closest to the ME tip (receiver piezo) monitors the displacement of the ME as an alternating voltage having a characteristic amplitude and phase.[30,31] When the tip-to-substrate distance is less than a few hundred nanometers, the oscillation of the ME is damped by shear forces between the ME tip, solution and substrate surface. The resulting amplitude damping and phase shifts of the receiver piezo are used in a feedback loop in order to maintain a constant tip-to-substrate separation. The overall geometry of the ME significantly affects the SF response,[32] thus requiring the use of a reproducible ME fabrication procedure to ensure comparable SF signals.[29,33] Optimization of the SF conditions has recently allowed height differences of 200–250 μm to be measured whilst simultaneously recording electrochemical data.[34]

To track the extensive depth profiles and accurately quantify bulk and local corrosion rates observed at corroded Mg materials, topography tracking

methodologies with an extended range must be developed for SECM applications. In the specific case of pure Mg and its alloys that have standard electrochemical potentials well below −1.5 V *vs.* SCE,[35] severe corrosion rates are expected (in the order of ~10–1000 mm per year[36] when galvanically coupled (depending on the other material) and <10 mm per year[12]as a standalone material), which impedes SECM studies. Weight loss[37,38] and H_2 collection[39] have been employed to measure bulk corrosion rates. They provide absolute amounts of corroded material but lack the ability to produce spatially resolved height profiles of the corroded substrate required in SECM. Microscopy techniques, such as confocal laser scanning microscopy[40] (CLSM) and laser-based profilometry,[41] have also been used to track local corrosion damage but would be difficult to interface with SECM, suffer from diffraction artifacts when a significant amount of corrosion product is present, and have a limited temporal resolution given their stop-go style experiments. Other alternatives include the scanning vibrating electrode technique (SVET), which measures local current densities *in situ* and approximate local corrosion rates using Faraday's law[41] and the scanning droplet cell method (SDC)[42] where the local corrosion rate measurement uses Tafel extrapolation of potentiodynamic polarization curves (PDPs).

We have prioritized the development of shear force (SF) probes because: (i) they have demonstrated excellent topographic performance in several media[43] and over a range of different samples;[19,44,45] (ii) the method is easily adaptable to a range of SECM sensors and (iii) it is capable of tracking the full range of topographic variations expected for corroding Mg materials. Herein, we present evidence that the SF methodology can accurately track topographical features relevant to the study of Mg material corrosion. In our current configuration, we can readily accommodate vertical features as small as 1 nm up to 40 mm. The SF methodology, illustrated here by *ex situ* measurements, can readily be applied during SECM measurements to produce both *in situ* reactivity and topographical data. We demonstrate a large working height range of 700 μm using SF on a severely corroded magnesium alloy-mild steel galvanic couple along with the topography of a microgalvanically corroded ZEK100 Mg alloy presenting microscopic scale features of less than 1.4 μm. The SF topography is benchmarked against conventional imaging techniques (profilometry and CLSM).

2 Experimental

2.1 Fabrication of micropipettes for constant distance imaging

Quartz capillaries of 0.3 mm internal diameter (ID) and 1 mm outer diameter (Sutter Instrument, Novato, CA) were washed in 0.1 M HNO_3 (Caledon Laboratories Ltd., Georgetown, Ont) for 2 hours, and dried overnight in an oven (95 °C). A P-2000 CO_2 laser puller (Sutter Instrument) was used to pull patch pipettes with an aperture of 500 nm diameter and taper length of 2.0 mm (measured along the pipette shaft from the tip to where ID = 0.15 mm).[8]

2.2 Mg alloys selected

Ingots of mild steel (MS), AE44 (composition: 91.6% = Mg, 4% = Al, 4% = rare earths elements, 0.4% other impurities) and ZEK100 (composition: 98% = Mg, 1% = Zn, <0.5% = rare earths elements, <0.5% = Zr) were received from General

Motors India Private Limited or General Motors Canada and cut down to 1.0 cm × 2.0 cm × 1.0 cm (length × width × thickness). AE44 and ZEK100 were selected since they are commercially available and used or envisioned for manufacturing automotive components.[15,46,47] The samples were then mounted in cold mounting epoxy (Epofix) (Struers, Ontario, Canada) and polished following an established procedure.[41] The AE44 and MS samples were placed one next to the other in galvanic contact, exhibiting no measurable resistance (<0.1 Ω), and mounted in epoxy and polished as for the single alloy.

2.3 Scanning droplet cell surface imaging

To perform the scanning droplet cell experiment over the polished ZEK100 sample, a micropipette was filled with an aqueous 1.6 wt% (0.6 M) NaCl solution. A Ag|AgCl reference wire (0.125 mm diameter Ag wire – GoodFellow Metals, Huntingdon, England), fabricated following an established procedure,[48] was inserted at the back of the micropipette. The polished ZEK100 sample was used as the WE in a two-electrode configuration. Upon surface wetting by the micropipette, the corrosion potential was recorded for 10 s. The micropipette was then lifted (10 μm) to break the electrical contact and repositioned to a new x,y coordinate and approached to the Mg alloy surface to perform a new corrosion potential measurement. This was repeated over a total width of 150 μm.

2.4 Corrosion of the galvanic couple and Mg alloy

Corroded surfaces were obtained by suspending the galvanic couple or ZEK100 face down in an aqueous (18.2 MΩ, Millipore Milli-Q Reference system) 1.6 wt% (0.6 M) NaCl (A.C.S. grade, ACP Chemicals, Montreal, Qc) solution, for 1 day. The accumulated corrosion product was removed through a 20 s immersion in gently agitated 1 M CrO_3 in water. The samples were then sonicated in methanol for 10 s to remove any surface excess of chromium solution and dried using an Ar stream. The alloys were stored in a desiccator to ensure complete dehydration.

2.5 Surface imaging using profilometry and CLSM

Depth profiles of the corroded AE44–MS galvanic couple were acquired with a non-contact profilometer using axial chromatism (CHR-150 – Nanovea 3D, 3.5 mm laser working distance, 30 Hz scanning frequency and 10 μm sample size).

Depth profiles of the ZEK100 sample following corrosion were measured through the detection of the reflected light intensity using an inverted objective Zeiss 510 confocal microscope equipped with a HeNe 633 nm laser. Depth profiles were extracted from the light intensities by considering how many steps of known distance (slices) through the focal plane, in the z-direction, were required to reach the deepest region. Maximum depths to achieve a focused image are reached at 30 μm. All samples had reference markers that enabled the same area of the sample to be measured by profilometry, CLSM and SF.

2.6 SF surface imaging parameters

SF tracking of corroded surfaces was achieved using a micropipette equipped with stimulation and receiver piezos (stimulation amplitude: 1 V; stimulation frequency: 274 kHz) and an ElProScan 1 SECM (HEKA, Germany; bipotentiostat

model PG340). The optimal stimulation frequency was identified by recording a frequency spectra with a tip-to-substrate separation greater than 500 nm above the substrate and with the tip in contact with the substrate (*vide infra*). To topographically image the corroded surfaces, the *z* approach was stopped when the SF amplitude decreased to 45% of the SF amplitude measured above the substrate at an approach speed of 10 nm s^{-1}. The height of both the stepper and *z* piezo were recorded and the tip was retracted 4 μm, before being repositioned to a new *x*,*y* coordinate.

3 Results and discussion

3.1 Monitoring microgalvanic corrosion of ZEK100 using a scanning droplet cell

The scanning droplet cell is a useful method to monitor the local corrosion rates of heterogeneous surfaces (Fig. 1a).[49] Mg alloys have a heterogeneous microstructure as secondary phases form during casting due to solubility limitations of

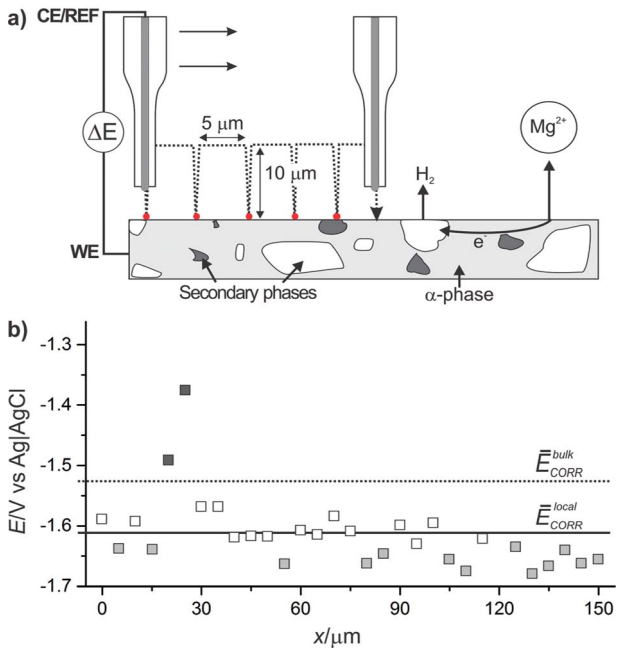

Fig. 1 (a) Schematic representation of the scanning droplet cell experiment performed to characterize the microgalvanic corrosion of Mg alloys. The polished Mg alloy was used as a WE and an Ag|AgCl CE/REF wire was inserted at the back of the micropipette. The red dots represent the electrical contacts between the electrolyte meniscus and the alloy surface. A hopping mode methodology was used with a retraction of 10 μm and motion in *x* of 5 μm; (b) corrosion potential measurements were performed over a ZEK100 Mg alloy using a filled micropipette with a 1.6 wt% NaCl solution over a line scan of 150 μm with 5 μm step size. The black, white and grey squares represent what is believed to be Zr particles, secondary Mg–Zn–Nd phase and α-phase, respectively. The average local E_{CORR} (full line) is −1.61 V, whereas the average bulk E_{CORR} (dotted line) is −1.53 V *vs.* Ag|AgCl.

the alloying elements in the Mg solid solution. The overall corrosion reaction of Mg materials can be simply described by the reactions,

$$Mg_{(s)} \rightarrow Mg^{2+}{}_{(aq)} + 2e^- \quad (1)$$

$$2H_2O_{(aq)} + 2e^- \leftrightarrows 2OH^-{}_{(aq)} + H_{2(g)} \quad (2)$$

$$Mg^{2+}{}_{(aq)} + 2OH^-{}_{(aq)} \leftrightarrows Mg(OH)_{2(s)} \quad (3)$$

In the case of ZEK100 Mg alloy, the microstructure comprises an α-Mg rich phase, a secondary Mg–Zn–Nd phase and Zr particles randomly distributed across its surface.[47] Some Zr particles have previously shown Fe enrichment, making them preferred cathodes and the location for water reduction (eqn (2)),[12] therefore driving the microgalvanic corrosion of ZEK100. As for the α-Mg matrix, due to its high Mg content, this phase is believed to dissolve producing Mg^{2+} ions (eqn (1)).

To highlight the microstructural heterogeneity of the polished ZEK100 Mg alloy, a scanning droplet cell experiment was performed to measure the local corrosion potential (E_{CORR}) using a micropipette filled with an aqueous 1.6 wt% NaCl solution, Fig. 1a. The measuring cycle entailed bringing the micro droplet into contact with the polished Mg alloy surface and measuring E_{CORR} *vs.* the Ag|AgCl CE/REF for 10 s to obtain an average value, before the contact was broken by retracting the pipette of 10 μm. The micropipette was subsequently displaced laterally by 5 μm to the next location and the measuring cycle was repeated, until a total displacement of 150 μm was reached. The results obtained are presented in Fig. 1b and showed a large variability in the measured E_{CORR}, with an average value of −1.61 V *vs.* Ag|AgCl (full line), which is lower than the reported macroscopic value of −1.53 V *vs.* Ag|AgCl (dotted line).[47] This variation of the measured local E_{CORR} (represented as black, grey and white squares in Fig. 1b) is consistent with an heterogeneous distribution of phases across the ZEK100 Mg alloy surface.[47] Interestingly, the E_{CORR} value of −1.38 V *vs.* Ag|AgCl, that was measured at $x = 25$ μm, is believed to be associated with a Zr particle. The size of the micropipette (500 nm aperture) used to perform this measurement is smaller then the size of these cathodic particles (<5 μm), thus isolating them for a local E_{CORR} measurement. These results are in agreement with previous results obtained by SKPFM, where Zr particles were shown to exhibit a Volta potential difference with the α-Mg-matrix of ∼180–250 mV.[50,51] The lower E_{CORR}, white squares, are believed to be associated with the secondary Mg–Zn–Nd phase while the grey squares, with the most negative E_{CORR}, are believed to be associated with the α-Mg matrix.

Given the restricted solvent window of the corroding solution, it is evident that the SDC methodology is useful in tracking the local E_{CORR} of a heterogeneous Mg alloy but lacks the capability to quantify local electrochemical fluxes generated by the ZEK100 microstructure. To track the Mg^{2+} release or molecular H_2 fluxes, micropotentiometric and microamperometric sensors, routinely used in SECM, are required. Currently, quantitative SECM studies of Mg materials are often restricted to corrosion initiation events where variations in topography are in the order of a few microns. This restriction is due to an inability to correlate the

material flux measured by the electrochemical probes with the observed local corrosion rates due to the lack of associated topographical information.

This situation is clearly unsatisfactory, so to quantify local corrosion rates occurring during microgalvanic corrosion and for galvanically coupled materials, a SF controlled SECM methodology was developed. This methodology can be easily adapted to a number of SECM uni- or multi-functional probes including amperometric MEs or potentiometric sensors.

3.2 SF controlled scanning micropipette method: positioning and calibration

SF sensitive frequencies are tip-to-substrate distance sensitive, making them ideal to probe surface topography and regulate the tip-to-substrate separation. The identification of these SF sensitive frequencies can be divided in three steps.[16,29]

First, a stimulation piezo and a receiver piezo, positioned 1–2 cm apart, were mounted on a pulled glass micropipette, Fig. 2(a)-(i). Secondly, a sinusoidal potential wave of a given frequency (f) was applied to the stimulation piezo, causing the micropipette to vibrate. With respect to the applied alternating voltage stimulus, of amplitude A_{in}, the response amplitude, A_{out}, and phase shift induced by mechanical oscillations of the micropipette were recorded at the receiver piezo (Fig. 2(a)-(ii)). The entire micropipette setup is brought in gentle contact ($\sim$50 nm) with the surface, where the SF sensitive frequencies are identified. To do so, a spectrum ranging from 250 to 300 kHz was obtained, Fig. 2(a)-(iii) (complete spectra are available in Fig. S1†). Comparison of the amplitude and phase monitored across the frequency spectra with the micropipette in contact with the surface (dashed lines in Fig. 2(a)-(iii)) revealed several frequencies that exhibited a significant decrease in amplitude and change in phase compared to when the micropipette was 500 nm above the surface (full lines in Fig. 2(a)-(iii)). These frequencies were assigned as SF sensitive. For each micropipette, a single SF sensitive frequency was selected and used in subsequent experiments. As schematically presented in Fig. 2b, along with the corresponding measurement, the amplitude and phase response of the selected SF sensitive frequency (in this case 274 kHz) was monitored while the micropipette was approached to the surface. Once in contact with the substrate (this is indicated by the complete attenuation of the amplitude signal), a calibration curve (Fig. 2c and the corresponding schematic representation) of the SF signal with an increasing tip-to-substrate distance was acquired by retracting the tip at 3 nm s^{-1}. From this curve, we selected the height set point used during topography tracking. This provided a quick and reliable approach to accurately monitor the tip-to-substrate separation.

This methodology can readily be applied to monitor topography across hard and soft (Fig. S2†) surfaces, using the 3-axis translator positioning system, and was first used to evaluate the microgalvanic corrosion of the ZEK100 Mg alloy followed by a study of the extent of corrosion damage over an AE44 Mg alloy galvanically coupled to MS, following one day of exposure to 1.6 wt% NaCl solution. For these samples, the set point defining the tip-to-substrate distance was set at 45% of the amplitude measured off the surface, giving a tip-to-substrate separation of less than 10 nm (separation between the attenuated amplitude signal point ($x = 0.039$ μm) and the red dot in Fig. 2c).

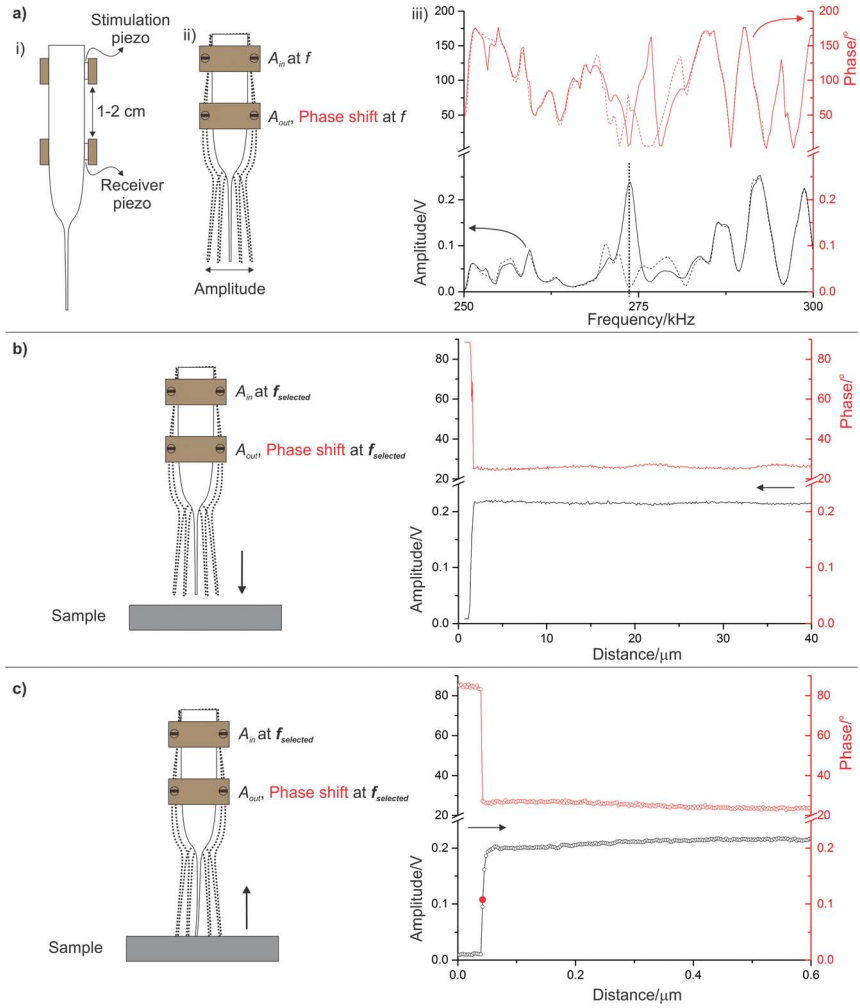

Fig. 2 (a) (i) Schematic representation of piezoelectric elements positioned on the shaft of the micropipette. (ii) Schematic representation of the parameters extracted (A_{in}, A_{out}, phase shift) from a SF spectrum. f represents the stimulation frequency. (iii) SF spectra recorded with a stimulation amplitude of 1 V when the micropipette is placed 500 nm above the surface (full line) and in contact with the surface (dashed line) for the phase (red curves) and amplitude signals (black curves). (b) Schematic representation of a SF approach curve and the corresponding approach curve at 1 μm s^{-1} in amplitude (A_{out}, black curve) and phase (phase shift, red curve) while exciting the stimulation piezo at 274 kHz ($f_{selected}$, dashed line in (a)-(iii)) with a stimulation amplitude of 1 V (A_{in}); (c) schematic representation of a SF calibration curve (pull back) and the corresponding measurement in amplitude (A_{out}, black curve) and phase (phase shift, red curve) recorded at 3 nm s^{-1} while exciting the stimulation piezo at the highlighted frequency and amplitude (A_{in}) in (a)-(iii) (274 kHz, $f_{selected}$); the threshold (45% of the surface amplitude) is highlighted by the dot on the amplitude curve.

3.3 Tracking ZEK100 microgalvanic corrosion depths using the SF constant distance mode

Mg and its alloys not only corrode when galvanically coupled but also as stand-alone materials. Although the severity of corrosion is far less when micro-galvanically corroding, (~10–1000 mm per year[36] when galvanically coupled *vs.* ~<10 mm per year[12]), it is mandatory that the SF methodology, in order to remain a competitive *ex situ* alternative, is able to track subtle microscopic features. To verify if SF has the capability of tracking microgalvanic corrosion features, a ZEK100 Mg alloy was corroded for a day and the corresponding SF results were benchmarked to standard CLSM.

The ZEK100 Mg alloy has previously been shown to exhibit filiform-like corrosion with networks interlinking secondary phases.[47] As observed by CLSM, filiform-like features are observed following a 24 h immersion of the ZEK100 in a 1.6 wt% NaCl aqueous solution, shown in Fig. 3a. From this micrograph, a height profile was extracted and is presented, Fig. 3b (top). Over the corrosion product film (mainly $Mg(OH)_2$, see eqn (3)), diffraction of the laser during CLSM was observed (for example at $x = 40$–80 μm), which limits the achievable resolution by

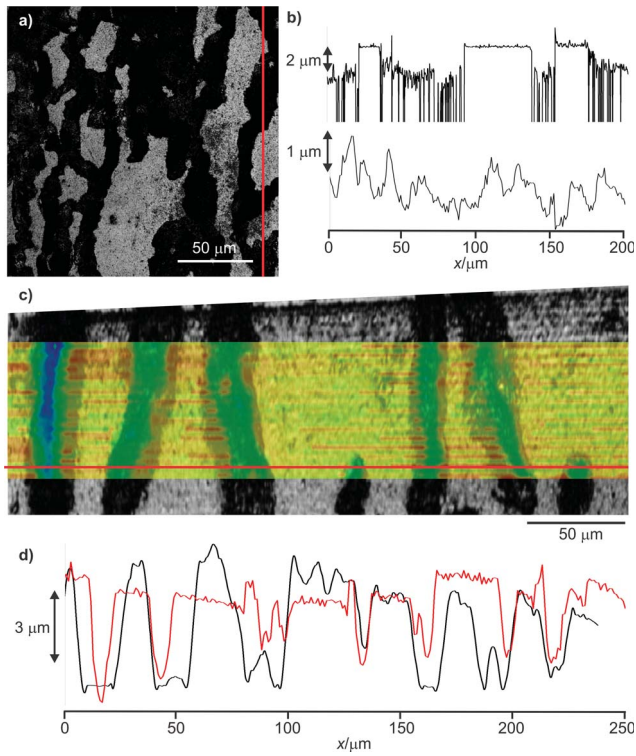

Fig. 3 (a) CLSM micrograph of a corroded ZEK100 Mg alloy corroded for 24 h in a 1.6 wt% NaCl aqueous solution with corrosion products present. (b) CLSM line scan along the red line in (a) (top) and SF line scan recorded across the area imaged by CLSM in (a) (bottom). (c) Topography map of the same area imaged by CLSM (black and white) and SF (color) with corrosion products removed. (d) Comparative SF (red curve) and CLSM (black curve) line scans recorded across the red line in (c).

CLSM. SF topography tracking can avoid those issues. As presented in Fig. 3b (bottom), a SF line scan was performed in the same region as the CLSM micrograph (Fig. 3a). Although it was not possible to relocate exactly where the line scan was taken on the CLSM micrograph, it is still possible to observe, by comparing the overall depth in Fig. 3b, that both line scans show features of similar heights (2–3 μm) and widths (10–20 μm). In addition, the micropipette tip was perfectly capable of tracking the surface covered by porous corrosion products.

To extract a depth profile of the microgalvanic corrosion process of ZEK100, the corrosion products were removed by immersing the sample in a chromium solution for 20 s. SF imaging of the sample was then performed, Fig. 3c (color map). Seven regions of lower heights were located over an area of 250 × 30 μm. These features were ~10–15 μm wide with a relative depth ranging from 3–5 μm, with a smaller feature of less than 1.5 μm deep. The tip of the micropipette was then used to mechanically scratch the sample, which served as a reference marker for subsequent CLSM measurements, Fig. 3c (black and white). Seven features with relative widths of ~10–15 μm were identified by CLSM and show good agreement with the corroded surface map acquired by SF, Fig. 3c. Fig. 3d shows a SF (red curve)/CLSM (black curve) comparative height measurement performed across the red line shown in Fig. 3c. Generally, cavity depths of ~3–5 μm were recorded by CLSM, which is in good agreement with the results obtained by SF. In some instances, depth differences were less than 100 nm (*e.g.* at $x = 140$ μm). However, over other locations (*e.g.* at $x = 55$ μm or $x = 180$ μm), SF underestimated the general corrosion of the material by ~3–5 μm. To improve the resolution obtained by SF, a smaller diameter micropipette and smaller step size should be used. The micropipette aperture has an outer diameter of ~700 nm, which sets a lower limit on the resolution. To properly track the corroded surface with SF, the micropipette is required to completely clear the edge before starting to move into the cavities. This explains why larger valleys are measured in CLSM in comparison to SF (Fig. 3d, $4 < x < 11$ μm). Finally, the corrosion rate (C_R) of the material was determined using:

$$C_R = \Delta z_m / t \quad (4)$$

where Δz_m is the maximum depth of corrosion after a time (t). Topography tracking by SF over the surface revealed that the ZEK100 should experience a corrosion rate in the order of 2.13 mm per year, evaluated from the deepest cavity. This result is within 5% of the corrosion rate of 2.24 mm per year evaluated for this sample by CLSM.

3.4 Tracking AE44–MS corrosion depths using the SF constant distance mode

An AE44–MS couple undergoes galvanic corrosion (Fig. 4a), where the metal with the higher reduction potential is referred to as the cathodic metal, which receives electrons from the metal with the lower reduction potential, the anodic metal. Since Mg has the lowest reduction potential,[52] it will corrode preferentially according to eqn (1)–(3).

The potential gradient is at its maximum at the AE44–MS interface and decays exponentially with increasing distance from that interface. Therefore, the most severe corrosion damage, and largest depth profile (630 μm) was expected at the AE44–MS material interface, with little corrosion damage anticipated on the MS surface.[41]

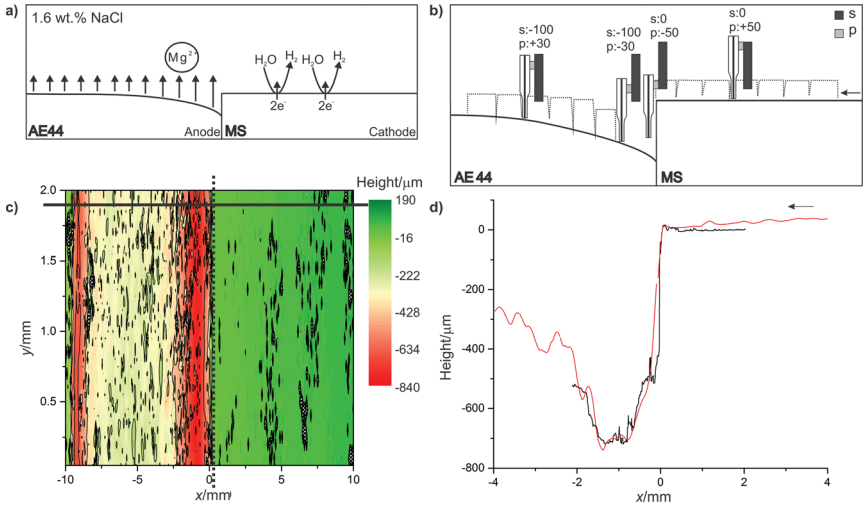

Fig. 4 (a) Schematic representation of an AE44–MS galvanic couple immersed in a 1.6 wt % NaCl solution generating Mg^{2+} at the anode and H_2 at the cathode; (b) stepper (s) and piezo (p) motor position schematic representation (not to scale), as the micropipette is scanned over the mixed material interface; (c) depth profile of a corroded 10–10 mm AE44–MS galvanic couple immersed in a 1.6 wt% NaCl solution for 24 hours, imaged using profilometry; the dashed line represents the interface between AE44 and MS; (d) line scan in SF (black line) and profilometry (red line) selected at $y = 1.95$ mm (highlighted full line shown in (c)). The negative distances represent the AE44 alloy while positive distances represent MS.

First, the topography was mapped by SF by scanning the micropipette from the MS towards the Mg alloy, using a frequency of 274 kHz and a stimulation amplitude of 1 V, as determined by the calibration measurement (Fig. 2c). As schematically represented in Fig. 4b, SF measurements were performed using a hopping mode methodology, where the micropipette was lowered at 10 nm s^{-1} towards the substrate and the approach stopped when the oscillation amplitude measured at the receiver piezo decreased from 0.2 V to 0.11 V. The height was recorded, before the micropipette was retracted 4 µm and moved to the next x,y coordinate. To achieve the large z travel distance suitable for measuring the steep edge due to galvanic coupling, translation of the probe was performed by the combination of the close looped z stepper motor and z piezo motion, providing a maximum z working distance of 40 mm. Here, the piezo motor had a maximum travel distance of 50 µm in the z direction. The approach was primarily performed using the piezo motor, however when it reached its maximal travel distance, the z stepper motor was used to reposition the micropipette at a suitable height for a z piezo approach. In this way changes in topography, which exceed the range of the piezo motor alone, can be accurately tracked (see piezo and stepper motor positions in Fig. 4b).

3.5 Evaluating the corrosion rate of galvanically coupled AE44

The extent of corrosion damage was first measured by profilometry using axial chromatism (Fig. 4c). In the presented case, a 10 µm sampling size was used to

obtain a large scan area. A maximum corrosion depth of 840 μm was observed along the AE44–MS interface ($x = 0$), which is in excellent agreement with previous studies performed under the same conditions.[36] The corrosion depth decreased with increasing distance from the interface until $x = -9$ mm where an increase in corrosion rate, consistent with an edge effect, was observed.[41] As with the CLSM experiments, diffraction effects were also observed during the profilometry experiment. The black areas observed in Fig. 4c represent spots where the non-contact profilometer suffered from diffraction artifacts.

Fig. 4d shows line scans acquired by SF (black line) and profilometry (red line) at the same location on the AE44–MS and showed excellent agreement. No significant topographical variations were observed between the techniques over the MS surface ($0 < x < 4$ mm). A maximal depth of 721 μm at the galvanic interface ($0 < x < -1$ mm) is obtained by SF and is within a 5% error of what is measured on the same sample by profilometry. As the tip moves away from the interface ($-1 < x < -4$ mm), the corrosion depth decreased due to the diminishing potential gradient.

In order to achieve a resolution similar to profilometry using SF, it has been reported by Etienne and co-workers that conical electrodes offer better tracking of tiny details present on a rough surface.[33] Following the same strategy, we used a 500 nm internal diameter aperture micropipette, which yielded more details of the scanned surface compared to profilometry, quantitatively providing a 2.7 times improved aspect ratio (3600 for SF *vs.* 1360 for profilometry).

The corrosion rate of AE44 was calculated from the profilometry and SF line scans in Fig. 4d, using eqn (4), for $t = 24$ h.[36] The comparatively large corrosion rate of 263 mm year^{-1} has been attributed to the large corrosion potential difference (ΔE_{CORR}) between AE44 and MS (~1 V), creating a polarized galvanic couple.[36] These data are in agreement with the previously reported corrosion rate of 243 mm year^{-1}.[36]

4 Conclusion

We have demonstrated that the SF methodology can accurately track millimeter and microscale topographical features over corroded samples. A micropipette was positioned at a constant distance above galvanically and microgalvanically corroded Mg alloys. Using a SF control set point to regulate the piezoelectric motors and by combining a long range stepper motor with the fine control of the piezoelectric motor, small (*ca.* 1.4 μm height over 250 μm lateral translation) and large depth profiles (*ca.* 0.72 mm height over 4 mm lateral translation) have been recorded. Importantly, this methodology was successful in tracking high aspect ratio features of a severely corroded AE44–MS galvanic couple. The resulting corrosion rate and depth profiles are consistent within 5% with *ex situ* profilometry and previous literature results. Similar agreement is obtained when comparing the corrosion rate of a ZEK100 Mg alloy, corroded for 24 h in the same solution and obtained by SF topography tracking, with that obtained by CLSM. The SF methodology was shown to be capable of acquiring the overall surface topography of a large area (250 × 30 μm) with excellent spatial resolution, showing the robustness of the technique.

The SF methodology presented can be readily applied during a SECM measurement to produce both *in situ* reactivity and topographical data. Moreover,

by using the SF methodology and dual probes, already envisioned for corrosion characterization, it will be possible to measure simultaneously several electrochemical fluxes while concomitantly tracking the surface topography. This concomitant knowledge is a prerequisite to the successful development of future SECM predictive numerical models.

Acknowledgements

This work was supported in part by the Natural Sciences and Engineering Research Council of Canada (NSERC) and General Motors of Canada. We thank Steen B. Schougaard for fruitful discussions. We thank Jon Carter and Justin Gammage from General Motors for providing the samples and helpful discussion. Luis Calzado, Monique Vasseur and Pellumb Jakupi are acknowledged for their technical expertise in profilometry and/or CLSM.

References

1 D. E. Tallman and M. B. Jensen, in *Scanning Electrochemical Microscopy*, CRC Press, 2nd edn, 2012, pp. 451–488.
2 L. Niu, Y. Yin, W. Guo, M. Lu, R. Qin and S. Chen, *J. Mater. Sci.*, 2009, **44**, 4511–4521.
3 M. V. Mirkin, W. Nogala, J. Velmurugan and Y. Wang, *Phys. Chem. Chem. Phys.*, 2011, **13**, 21196–21212.
4 K. Eckhard, M. Etienne, A. Schulte and W. Schuhmann, *Electrochem. Commun.*, 2007, **9**, 1793–1797.
5 M. Pähler, J. J. Santana, W. Schuhmann and R. M. Souto, *Chem.–Eur. J.*, 2011, **17**, 905–911.
6 J. J. Santana, M. Pähler, W. Schuhmann and R. M. Souto, *ChemPlusChem*, 2012, **77**, 707–712.
7 H. Krawiec, V. Vignal, O. Heintz, P. Ponthiaux and F. Wenger, *J. Electrochem. Soc.*, 2008, **155**, C127–C130.
8 P. Dauphin-Ducharme, R. M. Asmussen, D. W. Shoesmith and J. Mauzeroll, *J. Electroanal. Chem.*, 2015, **736**, 61–68.
9 J. Izquierdo, A. Kiss, J. J. Santana, L. Nagy, I. Bitter, H. S. Isaacs, G. Nagy and R. M. Souto, *J. Electrochem. Soc.*, 2013, **160**, C451–C459.
10 S. S. Jamali, S. E. Moulton, D. E. Tallman, M. Forsyth, J. Weber and G. G. Wallace, *Corros. Sci.*, 2014, **86**, 93–100.
11 W. Liu, F. Cao, Y. Xia, L. Chang and J. Zhang, *Electrochim. Acta*, 2014, **132**, 377–388.
12 P. Dauphin-Ducharme, R. Matthew Asmussen, U. M. Tefashe, M. Danaie, W. Jeffrey Binns, P. Jakupi, G. A. Botton, D. W. Shoesmith and J. Mauzeroll, *J. Electrochem. Soc.*, 2014, **161**, C557–C564.
13 U. M. Tefashe, M. E. Snowden, P. Dauphin-Ducharme, M. Danaie, G. A. Botton and J. Mauzeroll, *J. Electroanal. Chem.*, 2014, **720–721**, 121–127.
14 S. S. Jamali, S. E. Moulton, D. E. Tallman, M. Forsyth, J. Weber and G. G. Wallace, *Electrochim. Acta*, 2015, **152**, 294–301.
15 United States Automotive Materials Partnership, *Magnesium Vision 2020, A North American Automotive Strategic Vision for Magnesium*, Department of Energy National Energy Technology Laboratory, USA, 2004.

16 C. Cougnon, K. Bauer-Espindola, D. S. Fabre and J. Mauzeroll, *Anal. Chem.*, 2009, **81**, 3654–3659.
17 Y. Lee, Z. Ding and A. J. Bard, *Anal. Chem.*, 2002, **74**, 3634–3643.
18 H. Yamada, H. Fukumoto, T. Yokoyama and T. Koike, *Anal. Chem.*, 2005, **77**, 1785–1790.
19 Y. Takahashi, H. Shiku, T. Murata, T. Yasukawa and T. Matsue, *Anal. Chem.*, 2009, **81**, 9674–9681.
20 A. Kueng, C. Kranz, A. Lugstein, E. Bertagnolli and B. Mizaikoff, *Angew. Chem., Int. Ed.*, 2003, **42**, 3238–3240.
21 A. Davoodi, J. Pan, C. Leygraf and S. Norgren, *Electrochim. Acta*, 2007, **52**, 7697–7705.
22 A. Davoodi, J. Pan, C. Leygraf and S. Norgren, *J. Electrochem. Soc.*, 2008, **155**, C211–C218.
23 D. Ruhlig and W. Schuhmann, *Electroanalysis*, 2007, **19**, 191–199.
24 J. Izquierdo, S. González and R. M. Souto, *Int. J. Electrochem. Sci.*, 2012, **7**, 11377–11388.
25 P. M. Diakowski and Z. Ding, *Electrochem. Commun.*, 2007, **9**, 2617–2621.
26 K. Borgwarth, D. Ebling and J. Heinze, *Electrochim. Acta*, 1995, **40**, 1455–1460.
27 M. Ludwig, C. Kranz, W. Schuhmann and H. E. Gaub, *Rev. Sci. Instrum.*, 1995, **66**, 2857–2860.
28 A. Hengstenberg, C. Kranz and W. Schuhmann, *Chem.–Eur. J.*, 2000, **6**, 1547–1554.
29 L. Danis, M. E. Snowden, U. M. Tefashe, C. N. Heinemann and J. Mauzeroll, *Electrochim. Acta*, 2014, **136**, 121–129.
30 B. Ballesteros Katemann, A. Schulte and W. Schuhmann, *Chem.–Eur. J.*, 2003, **9**, 2025–2033.
31 B. Ballesteros Katemann, A. Schulte and W. Schuhmann, *Electroanalysis*, 2004, **16**, 60–65.
32 M. Etienne, S. Lhenry, R. Cornut and C. Lefrou, *Electrochim. Acta*, 2013, **88**, 877–884.
33 M. Etienne, J.-P. Moulin and S. Gourhand, *Electrochim. Acta*, 2013, **110**, 16–21.
34 M. Etienne, B. Layoussifi, T. Giornelli and D. Jacquet, *Electrochem. Commun.*, 2012, **15**, 70–73.
35 T. Cain, L. G. Bland, N. Birbilis and J. R. Scully, *Corrosion*, 2014, **70**, 1043–1051.
36 K. B. Deshpande, *Corros. Sci.*, 2010, **52**, 3514–3522.
37 A. D. Sudholz, K. Gusieva, X. B. Chen, B. C. Muddle, M. A. Gibson and N. Birbilis, *Corros. Sci.*, 2011, **53**, 2277–2282.
38 R. Matthew Asmussen, W. Jeffrey Binns, P. Jakupi and D. Shoesmith, *J. Electrochem. Soc.*, 2014, **161**, C501–C508.
39 A. D. King, N. Birbilis and J. R. Scully, *Electrochim. Acta*, 2014, **121**, 394–406.
40 R. M. Asmussen, P. Jakupi, M. Danaie, G. A. Botton and D. W. Shoesmith, *Corros. Sci.*, 2013, **75**, 114–122.
41 D. Trinh, P. Dauphin Ducharme, U. Mengesha Tefashe, J. R. Kish and J. Mauzeroll, *Anal. Chem.*, 2012, **84**, 9899–9906.
42 H. Böhni, T. Suter and A. Schreyer, *Electrochim. Acta*, 1995, **40**, 1361–1368.
43 A. P. Sommer and R. P. Franke, *Micron*, 2002, **33**, 227–231.
44 M. Etienne, E. C. Anderson, S. R. Evans, W. Schuhmann and I. Fritsch, *Anal. Chem.*, 2006, **78**, 7317–7324.

45 M. Etienne, A. Schulte, S. Mann, G. Jordan, I. D. Dietzel and W. Schuhmann, *Anal. Chem.*, 2004, **76**, 3682–3688.
46 J. Min, L. Hector Jr, J. Lin and J. Carter, *J. Mater. Eng. Perform.*, 2013, **22**, 3324–3336.
47 R. M. Asmussen, W. J. Binns, P. Jakupi and D. Shoesmith, *Corrosion*, 2015, **71**, 242–254.
48 T. J. Smith and K. J. Stevenson, in *Handbook of Electrochemistry*, ed. C. G. Zoski, Elsevier, Amsterdam, 2007, pp. 73–110.
49 H. Krawiec, S. Stanek, V. Vignal, J. Lelito and J. S. Suchy, *Corros. Sci.*, 2011, **53**, 3108–3113.
50 M. F. Hurley, C. M. Efaw, P. H. Davis, J. R. Croteau, E. Graugnard and N. Birbilis, *Corrosion*, 2015, **71**, 160–170.
51 A. E. Coy, F. Viejo, P. Skeldon and G. E. Thompson, *Corros. Sci.*, 2010, **52**, 3896–3906.
52 A. S. G82–98, *Annual Book of ASTM Standards, Development and Use of a Galvanic Series for Predicting Galvanic Corrosion Performance*, ASTM International, Philadelphia, 2003.